Chemical Engineering Journal 415 (2021) 128904

Contents lists available at ScienceDirect

Chemical Engineering Journal

journal homepage: www.elsevier.com/locate/cej

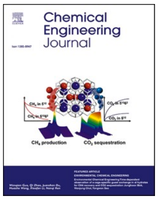

Composition manipulation of bis(fluorosulfonyl)imide-based ionic liquid electrolyte for high-voltage graphite//$LiNi_{0.5}Mn_{1.5}O_4$ lithium-ion batteries

Purna Chandra Rath [a,‡], Yi-Wun Wang [b,‡], Jagabandhu Patra [a,c], Bharath Umesh [b], Ting-Ju Yeh [d], Shigeto Okada [e], Ju Li [f], Jeng-Kuei Chang [a,b,c,e,*]

[a] *Department of Materials Science and Engineering, National Yang Ming Chiao Tung University, 1001 University Road, Hsinchu 30010, Taiwan*
[b] *Institute of Materials Science and Engineering, National Central University, 300 Jhong-Da Road, Taoyuan 32001, Taiwan*
[c] *Hierarchical Green-Energy Materials (Hi-GEM) Research Center, National Cheng Kung University, 1 University Road, Tainan 70101, Taiwan*
[d] *Department of Energy Nanomaterials, Material & Chemical Research Laboratory, Industrial Technology Research Institute, Hsinchu 31040, Taiwan*
[e] *Institute for Materials Chemistry and Engineering, Kyushu University, Fukuoka 816-8580, Japan*
[f] *Department of Nuclear Science and Engineering and Department of Materials Science and Engineering, Massachusetts Institute of Technology, 77 Massachusetts Avenue, Cambridge, MA 02139, USA*

A R T I C L E I N F O

Keywords:
Electrolyte design
High-voltage cathode
Al corrosion
Battery safety
5-V battery

A B S T R A C T

Ionic liquids (ILs), with wide electrochemical stability window, high thermal stability, and nonvolatility, are promising electrolytes for lithium-ion batteries. Among ILs with various types of anion, bis(fluorosulfonyl)imide (FSI^-)-based ILs are particularly appealing owing to their high ionic conductivity, low viscosity, and great anode compatibility. However, strong corrosivity of FSI^- toward the Al current collector at high potential restricts their practical utilization. In this study, three strategies are implemented to overcome this limitation. Li^+ fraction modulation, FSI^-/bis(trifluoromethyl)sulfonylimide ($TFSI^-$) molar ratio optimization, and their synergistic combination are used to achieve optimal charge–discharge of a high-voltage $LiNi_{0.5}Mn_{1.5}O_4$ (LNMO) cathode with an Al substrate. The effects of the IL composition on the electrochemical properties of a graphite anode are also investigated. The proposed IL electrolyte, which lacks any organic solvents, has an optimal $Li^+/FSI^-/TFSI^-$ molar ratio and thus can effectively suppress the Al corrosion, allowing a 5-V graphite//LNMO full cell to be realized. A reversible capacity of ~ 135 mAh g^{-1} (based on LNMO) and a capacity retention of ~ 85% after 200 cycles are found for the full cell. This study opens a new route for FSI^--based IL electrolytes in the field of high-voltage and high-safety lithium-ion battery applications.

1. Introduction

Lithium-ion batteries (LIBs) are widely used in consumer applications as well as large-scale grid implementations owing to their adequate gravimetric and volumetric capacities, long life, and low maintenance cost [1,2]. Nevertheless, with surging demand for energy storage, state-of-the-art LIBs fall short of meeting the requirements of energy and power densities as well as operational safety [3]. To improve the energy density of LIBs, besides increasing the specific capacities of the anode and cathode materials, enhancing the cell voltage is vital [4,5]. In this context, several high-voltage (>4.5 V) cathodes are currently being pursued, such as lithium-rich layered oxides ($Li_{1+x}M_{1-x}O_2$, M = Mn, Ni, Co, etc.), spinel oxides (e.g., $LiNi_{0.5}Mn_{1.5}O_4$ (LNMO)), and polyanionic compounds (e.g., $LiCoFePO_4$, Li_2NiPO_4, Li_2CoPO_4F, etc.) [6–8]. The electrolyte is a critical component in high-voltage LIBs [9,10]. The conventional carbonate electrolyte with $LiPF_6$ is unsuitable for high-voltage applications [11,12]. The insufficient electrochemical stability of the carbonate solvent restricts operation beyond ~ 4.3 V (vs. Li^+/Li), where anodic decomposition of the electrolyte takes place [13]. Moreover, the solvent is thermally unstable, highly volatile, and flammable [13]. In addition, $LiPF_6$ is not an ideal Li salt because of its poor thermal stability and high moisture sensitivity [14]. Highly reactive species, including POF_3, PF_5, and HF, are easily generated and subsequently damage the electrodes, solid electrolyte interphase (SEI), and other battery components [15]. The development of high-voltage electrolytes with superior reliability and safety is thus required. It is noted that to

---

* Corresponding author.
E-mail address: jkchang@nctu.edu.tw (J.-K. Chang).
‡ PCR and YWW contributed equally to this work.

https://doi.org/10.1016/j.cej.2021.128904
Received 24 September 2020; Received in revised form 29 January 2021; Accepted 5 February 2021

improve LIB performance, tuning the electrolyte composition is much easier than developing sophisticated electrode materials and engineering their architectures.

Room-temperature ionic liquids (ILs) are a promising type of LIB electrolyte due to their wide electrochemical stability window, high thermal stability, nonvolatility, and environmental friendliness [16,17]. Various combinations of organic cations (e.g., imidazolium, pyridinium, phosphonium, ammonium, and pyrrolidinium) and anions (e.g., hexafluoro-phosphate, tetrafluoroborate, bis(trifluoromethyl)sulfonylimide ($TFSI^-$), bis(fluorosulfonyl)imide (FSI^-), and dicyanamide) have been adopted to tailor ILs for diverse applications, such as electrodeposition, batteries, solar cells, supercapacitors, fuel cells, actuators, water splitting, thermal storage, CO_2 capture/separation, etc [18–21]. However, compared to the conventional carbonate electrolyte, ILs usually have higher viscosity and lower ionic conductivity, leading to unsatisfactory wettability toward LIB separators and electrodes [22,23]. One strategy to overcome these problems is to form an IL-based hybrid electrolyte by incorporating a low-viscosity organic solvent to enhance ion transport [24,25]. However, the safety and stable potential window of hybrid electrolytes are compromised by the presence of an organic solvent [26,27]. Several research groups have demonstrated the feasibility of using plain IL electrolytes (without an organic solvent) to enhance the elevated-temperature performance and cycle life of LIB electrodes [28–30]. TFSI-based ILs are most commonly used for this task [31,32]. Recently, FSI-based ILs have become increasingly attractive owing to their considerably lower viscosity, higher ionic conductivity, and better SEI forming ability compared to those of their TFSI counterparts [33,34]. However, to the best of our knowledge, the utilization of FSI-based IL electrolytes for high-voltage cathodes has not been achieved.

IL electrolytes based on FSI^- anions have been proven promising for $LiFePO_4$ and layer-structure oxide cathodes, which have relatively low redox potentials. For example, Salem *et al.* studied the electrochemical behavior of phosphonium-based ILs and found that ILs with FSI^- anions performed well with a $LiFePO_4$ cathode but failed with an LNMO cathode (which has a charge–discharge plateau at ~ 4.7 V vs. Li^+/Li) [35]. Zhang *et al.* demonstrated that a $LiCoO_2$ cathode has good cycling stability (~70 cycles) at 60 °C in LiTFSI/*N*-propyl-*N*-methylpyrrolidinium − FSI (PMP − FSI) IL electrolyte [36]. Yamaguchi *et al.* showed the improved electrochemical properties of Li/$LiCoO_2$ cells with the LiTFSI/PMP − FSI electrolyte containing a zwitterion additive [37]. Heist *et al.* demonstrated the superior stability and rate performance of a $LiNi_{0.8}Mn_{0.1}Co_{0.1}O_2$ half cell with a highly concentrated LiFSI/PMP − FSI IL electrolyte [38]. Liu *et al.* studied *N*-methyl-*N*-propylpiperidinium − FSI IL electrolytes with various LiFSI concentrations and demonstrated that a $LiNi_{0.5}Mn_{0.3}Co_{0.2}O_2$/Li cell can deliver an optimal capacity of 152 mAh g^{-1} at room temperature [39]. It is noted that the operation potentials of the above-mentioned cathodes are below 4.5 V. Beyond this potential, corrosion of the Al substrate (i.e., cathode current collector), due to the presence of FSI^-, occurs, leading to cell failure [40,41]. This is a major hurdle for FSI^--based IL electrolytes. Better electrolyte recipes are thus needed to suppress Al corrosion to realize high-voltage LIB applications.

To achieve high-energy–density LIBs, besides the cathode properties, good anode performance is essential. This means that while designing an electrolyte composition for a battery cathode, the corresponding anode properties should also be considered. Many previous high-voltage electrolyte studies focused on the optimization of cathode performance, often overlooking anode compatibility. A rational electrolyte design that takes into account both cathode and anode properties for a 5-V LIB full cell is examined in the present work.

In this study, a systematic investigation of the electrolyte composition of PMP − FSI-based ILs is conducted to enable the implementation of a high-voltage LNMO cathode. Three electrolyte design strategies are adopted. First, the LiFSI salt concentration is manipulated to control the Li^+ fraction in the IL electrolyte. Second, $TFSI^-$ anions are incorporated. The $FSI^-/TFSI^-$ molar ratio is modulated to adjust the physicochemical properties of the electrolytes and their corrosivity toward Al. Third, synergistic controls of both Li^+ fraction and $FSI^-/TFSI^-$ ratio are combined. The proposed 2.4 m LiTFSI/PMP − FSI electrolyte, which lacks any organic solvents, has excellent compatibility with a graphite anode and allows an LNMO cathode to have great rate capability and cyclability. A practical 5-V graphite//LNMO full cell with this electrolyte is demonstrated. This cell has a high capacity of 135 mAh g^{-1} (based on the LNMO mass) and a satisfactory capacity retention of ~ 85% after 200 charge–discharge cycles.

2. Experimental section

2.1. Preparation of LNMO and electrolytes

A co-precipitation method was used to synthesize LNMO powder; the details can be found in a previous paper [42]. Briefly, an aqueous solution with stoichiometric amounts of $NiSO_4{\cdot}6H_2O$ and $MnSO_4{\cdot}H_2O$ was slowly injected into a reaction vessel, which was maintained at 50 °C. An NH_4OH and NaOH solution was used to control the pH at ~ 10.5. $Ni_{0.25}Mn_{0.75}(OH)_2$ particles with a diameter of ~ 10–15 μm precipitated. The $Ni_{0.25}Mn_{0.75}(OH)_2$ was mixed with Li_2CO_3 and calcined at 750 °C in air for 12 h, yielding LNMO powder. Graphite powder (MG-16) was received from China Steel Chemical Corporation, Taiwan.

PMP − FSI and PMP − TFSI ILs (purity: 99.9%), purchased from Solvionic, were vacuum-dried at 80 °C for 24 h before use. Battery-grade LiFSI and LiTFSI were purchased from Kishida Chemical. A conventional electrolyte, consisting of 1 M $LiPF_6$ in ethylene carbonate (EC)/diethyl carbonate (DEC) (1:1 by volume) mixed solvent, was used for comparison. All the electrolytes were prepared in a glove box and dried over fresh molecular sieves before use. The water content of the electrolytes, measured using a Karl Fisher titrator, was below 25 ppm.

2.2. Cell assembly

The electrode slurry was fabricated by mixing the active material (LNMO or graphite powder), super P, and poly(vinylidene fluoride) binder in a weight ratio of 80:10:10 in *N*-methyl-*2*-pyrrolidone solution. The slurry was cast onto an Al or Cu current collector using a doctor blade and then vacuum-dried at 100 °C for 12 h. The obtained electrode was roll-pressed and punched to match the required circular dimension of a CR2032 coin cell. The active material loading amounts of LNMO and graphite were ~ 4 and ~ 1.9 mg cm^{-2}, respectively. Li foil and a glass fiber membrane were used as the counter electrode and the separator, respectively. The assembly of the coin cells was done in an argon-filled glove box (Innovation Technology Co. Ltd.) with both water and oxygen content levels below 0.3 ppm.

2.3. Material and electrochemical characterization

The sample morphology and microstructure were analyzed using scanning electron microscopy (SEM; FEI Inspect F50) and transmission electron microscopy (TEM; FEI Tecnai F20). The crystallinity of the synthesized LNMO was examined using X-ray diffraction (XRD; Bruker D8). Thermogravimetric analysis (TGA; Perkin-Elmer TGA7) was employed to evaluate the thermal stability of the electrolytes. The coordination states of various electrolytes were investigated with Raman spectroscopy (LabRAM HR 800 with a laser wavelength of 633 nm). The electrolyte flammability was tested following the procedures suggested in a previous study [26]. Briefly, the electrolyte was adsorbed in a glass fiber membrane and then heated with an electric Bunsen burner under air. The distance between the sample and the flame was 123 mm. The contact angle measurements were conducted using a static sessile drop method and recorded with a digital goniometer. Electrochemical impedance spectroscopy (EIS) and Linear sweep voltammetry (LSV) were carried out with a Biologic VSP-300 potentiostat. EIS measurements were carried out in a frequency range of 10^6–10^{-2} Hz with an AC amplitude of 10 mV. The galvanostatic charge–discharge properties (such as capacity, rate capability, and cycling stability) of the cells were evaluated using an Arbin BT-2043 battery tester. For the graphite//LNMO full cell, an anode/cathode capacity ratio of ~ 1.2 was used. The graphite anode was pre-conditioned for three cycles in a half cell and then assembled in the full cell.

3. Results and discussion

Fig. 1**(a)** shows that the synthesized spherical LNMO particles consisted of numerous rod-like structures. The spinel-type crystallinity (JCPDS-80-2184) of the LNMO is confirmed by the XRD pattern shown in Fig. 1**(b)**, which exhibits no impurity phases. Fig. 1**(c)** shows a high-resolution TEM image, in which a highly ordered LNMO lattice can be observed. The fringe spacing of 4.7 Å is associated with the LNMO (1 1 1) plane distance. The electron diffraction pattern in **Fig. S1(a)** confirms the cubic spinel structure. The array of diffraction spots can be ascribed to various LNMO crystal planes, as indexed in the figure. The extra diffraction signals with weaker intensity between the major diffraction spots reflect the existence of Ni/Mn ordering in the LNMO lattice [43,44] As shown in the Raman spectrum in **Fig. S1(b)**, a clear splitting of the $F^1{}_{2g}$ band is found at 598 and 621 cm^{-1}, which is characteristic of the $P4_332$ space-group symmetry of LNMO [45]. The well-ordered Ni and Mn atoms in the LNMO lattice are confirmed by the noticeable peaks at 165 and 210 cm^{-1} [45]. These results are consistent with the TEM observation.

The electrochemical stability windows of the conventional $LiPF_6$/EC/DEC electrolyte and the 0.8 m LiFSI/PMP − FSI electrolyte were measured with Pt electrodes; the data are shown in Fig. 2**(a)**. The anodic decomposition potentials were found to be ~ 4.2 and ~ 5.2 V (vs. Li^+/Li), respectively, indicating the superior stability of the IL electrolyte. Fig. 2**(b)** shows the TGA results for the two electrolytes. A significant weight loss of the conventional electrolyte was observed below 100 °C, where the EC/DEC solvent violently evaporated and the $LiPF_6$ decomposed into LiF and PF_5 [14,15]. Before 200 °C, all the electrolyte was burnt off and there was nothing left on the TGA crucible. In contrast, the IL electrolyte exhibited much better thermal stability and lower volatility. The main decomposition reaction occurred at ~ 310 °C. **Fig. S2** shows the flammability testing data, which indicate that the IL electrolyte is less flammable. The immersion test results of LNMO powder in the two electrolytes are shown in Fig. 2**(c)**. Noticeable Mn and Ni dissolutions were found in the carbonate electrolyte, probably due to the attack of HF and PF_5 toward LNMO [46]. In contrast, little dissolution of these elements was found in the IL electrolyte. Fig. 2**(d)** compares the chronoamperometry data of Al electrodes recorded in the two electrolytes at 5 V. Al passivation was recognized in the $LiPF_6$/EC/DEC electrolyte, whereas the anodic current continuously increased with time in the LiFSI/PMP − FSI IL. The SEM image in Fig. 2**(e)** confirms that this substantial anodic current was related to Al pitting corrosion. The FSI^- anions are prone to react with Al, forming soluble Al − FSI complexes [40,47]. This is the major challenge for FSI-based IL electrolytes for practical high-voltage LIB applications. Fig. 2**(f)** shows the charging curve of the LNMO half cell with the 0.8 m LiFSI/PMP − FSI IL electrolyte. The charging process failed to reach the cut-off voltage due to the severe Al corrosion side reaction.

3.1. *Effects of Li^+ fraction*

Recently, several research works have demonstrated that a high concentration of Li salt can effectively alleviate Al corrosion [36,39]. Hence, we prepared PMP − FSI IL electrolytes with various concentrations of LiFSI. Raman spectroscopy was used to examine the electrolyte coordination structures. The obtained spectra in Fig. 3**(a)** reveal distinct Raman bands in the region of 700–780 cm^{-1}, corresponding to the various coordination statuses of FSI^- [48]. The bands at 720, 732, 746,

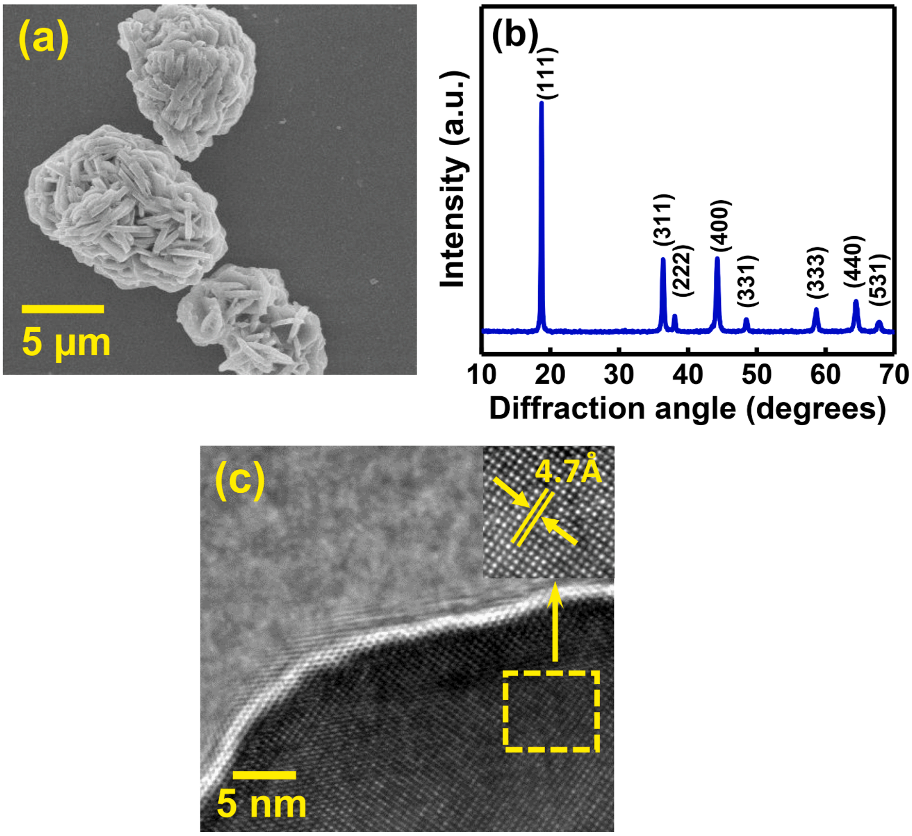

Fig. 1. (a) SEM image, (b) XRD pattern (c) high-resolution TEM image of synthesized LNMO powder.

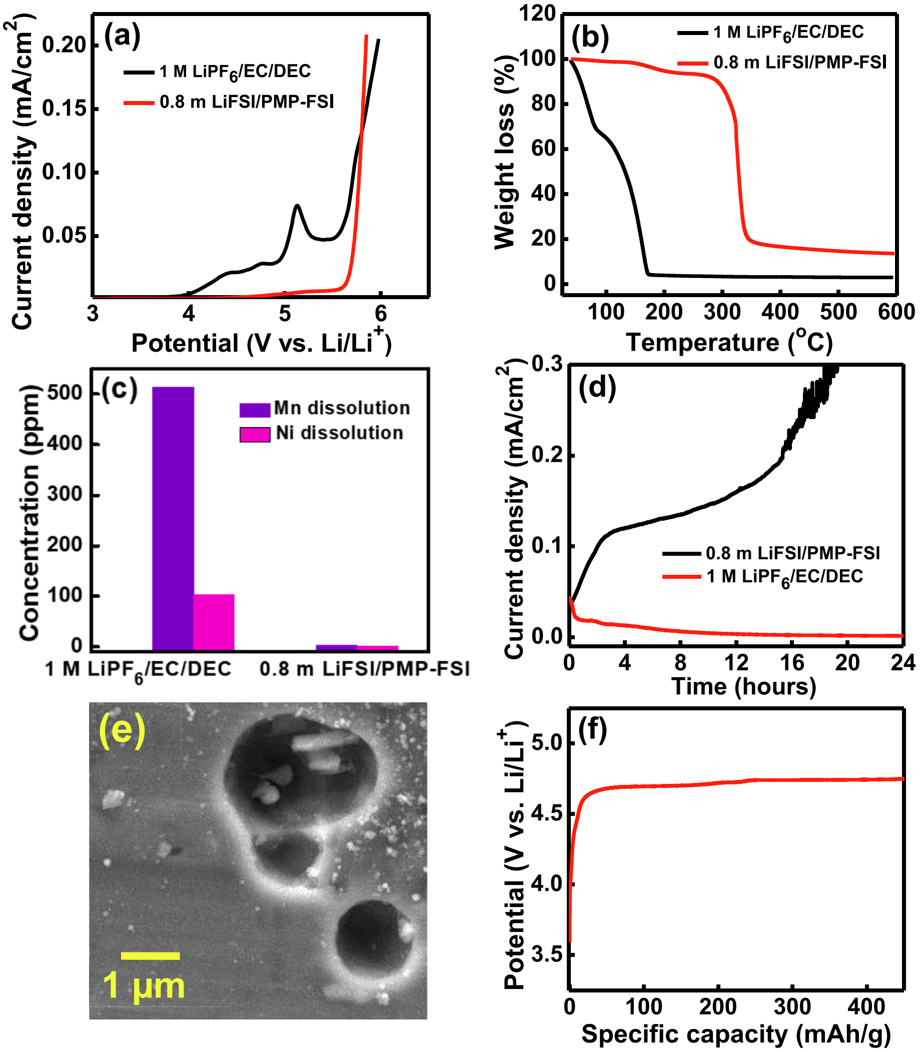

Fig. 2. (a) LSV curves of Pt electrodes recorded at potential scan rate of 1 mV s^{-1}. (b) TGA data of electrolytes. (c) Dissulution data of 0.5 g LNMO powder in 2 mL electrolyte after 1 month. (d) Chronoamperometry data of Al electrodes recorded at 5 V in two electrolytes. (e) SEM image of Al electrode after chronoamperometry test in 0.8 m LiFSI/PMP – FSI electrolyte. (f) Charging curve of LNMO half cell with 0.8 m LiFSI/PMP–FSI electrolyte.

and 760 cm^{-1} can be assigned to the free FSI$^-$, contact ion pair (CIP, an FSI$^-$ ion coordinated to a Li$^+$ ion), ion aggregate type I (AGG-I, an FSI$^-$ ion coordinated with two Li$^+$ ions), and ion aggregate type II (AGG-II, an FSI$^-$ ion coordinated with more than two Li$^+$ ions), respectively [48,49]. The interaction between the sulfonyl oxygens and nitrogen in FSI$^-$ and the Li$^+$ ions modifies the FSI$^-$ stretching features, varying the Raman wavenumbers [50,51]. As shown, with increasing LiFSI concentration, the overall Raman peak shifts toward a higher wavenumber, indicative of the promoted formation of AGG-I and AGG-II. Because there are fewer free FSI$^-$ anions to attack Al, the LSV anodic current was suppressed at a high concentration of LiFSI, as shown in Fig. 3**(b)**. Accordingly, a high Li$^+$ fraction in the PMP – FSI IL electrolyte can mitigate Al dissolution to a certain extent. However, the SEM image in Fig. 3**(c)** reveals that even with 3.2 m LiFSI, which is close to the solubility limit, clear Al pitting corrosion can be observed. Fig. 3**(d)** shows the charge–discharge curves of the LNMO half cell with the 3.2 m LiFSI/PMP – FSI IL electrolyte. Because of the side reaction of Al dissolution, the apparent charge capacity was higher than the theoretical LNMO capacity and poor charge–discharge Coulombic efficiency (CE) was obtained. This high-LiFSI-concentration IL electrolyte is thus unfavorable for high-voltage operation. A better electrolyte recipe is needed.

3.2. Effects of FSI$^-$/TFSI$^-$ molar ratio

We adjusted the FSI$^-$/TFSI$^-$ molar ratio in the IL electrolyte while keeping the Li$^+$ concentration at 0.8 m. FSI$^-$/TFSI$^-$ ratios of 3:1, 1:1, and 1:3 are denoted as FT-31, FT-11, and FT-13, respectively. Fig. 4**(a)** shows the Raman spectra of the electrolytes. Besides FSI$^-$ bands, the uncoordinated (free), CIP, and AGG states of TFSI$^-$ were observed. Given a similar coordination status, the TFSI$^-$ vibrational wavenumber is higher than that for FSI$^-$ [52]. As a consequence, a positive shift of the Raman peak with increasing TFSI$^-$ ratio was found. **Fig. S3** shows the TGA data for the FT-13 electrolyte. Because the thermal stability of TFSI$^-$ species is superior to that of FSI$^-$ species [53], the bulk decomposition temperature (i.e., above 400 °C) of this FT-13 electrolyte is higher than that of the LiFSI/PMP – FSI electrolyte (see Fig. 2**(b)**). As shown in Fig. 4**(b)**, the incorporation of TFSI$^-$ significantly contributes to the suppression of Al corrosion. The LSV anodic current decreased with increasing TFSI$^-$/FSI$^-$ ratio. The TFSI$^-$ anions either are inactive with air-formed Al_2O_3 or react with Al to generate stable and insoluble Al–TFSI species in the IL electrolyte, which passivates the electrode surface and thus reduces the attack from FSI$^-$ anions [54,55]. As shown in the SEM micrographs in Fig. 4**(c)–(e)**, Al pitting corrosion still occurred with the FT-31 and FT-11 electrolytes, but was effectively eliminated with the FT-13 electrolyte.

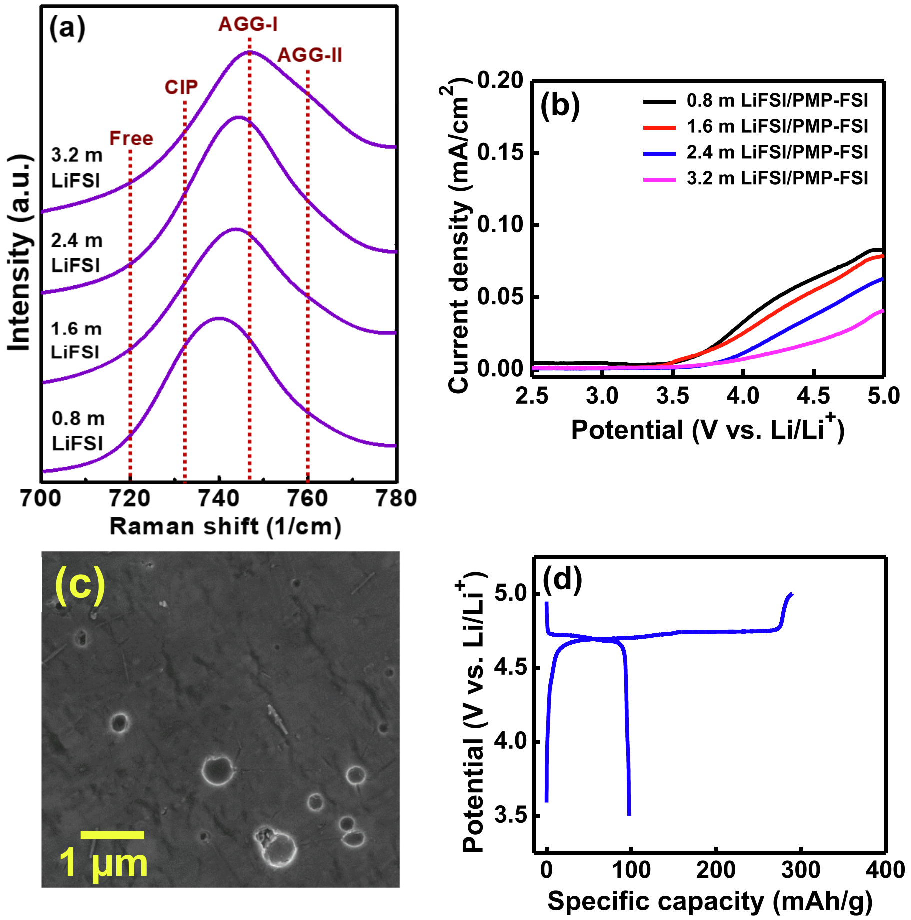

Fig. 3. (a) Raman spectra of PMP–FSI electrolytes with various concentrations of LiFSI. (b) LSV curves of Al electrodes recorded in various electrolytes. (c) SEM image of Al electrode after chronoamperometry test in 3.2 m LiFSI/PMP–FSI electrolyte. (d) Charge-discharge curve of LNMO half cell with 3.2 m LiFSI/PMP–FSI electrolyte.

The progressive inhibition of Al corrosion with the cumulative addition of TFSI$^-$ content clearly affected the electrochemical performance of the LNMO cells. With the FT-31 electrolyte, the LNMO cell was unable to complete a single charge–discharge cycle due to relatively serious Al corrosion. As shown in Fig. 5**(a)**, with the FT-11 electrolyte, the charge–discharge CE is still unsatisfactory, and continuous discharge capacity fading can be seen. When the TFSI$^-$ content was further increased (i.e., FT-13 electrolyte), much improved electrochemical properties were observed. Fig. 5**(b)** shows that the discharge capacity of LNMO at 0.1C is as high as 130 mAh g^{-1}. The charge–discharge performance and CE are much better than those obtained with the high-concentration 3.2 m LiFSI/PMP − FSI electrolyte (Fig. 3**(d)**). Although this is the first FSI-containing IL electrolyte that allows successful operation of a high-voltage LNMO cathode, we are not completely satisfied with the electrode rate capability. As shown in Fig. 5**(b)**, the measured discharge capacity at 2C was only 70 mAh g^{-1}, corresponding to ~ 54% retention as compared to the capacity at 0.1C. The charge–discharge properties of a graphite half cell with the FT-13 electrolyte were also evaluated. The data obtained are shown in Fig. 5**(c)**. The delithiation capacity of the graphite electrode dramatically decreased from 325 mAh g^{-1} at 0.1C to below 100 mAh g^{-1} at 0.3C. The inferior high-rate performance is associated with the highly resistive SEI layer that formed in the high-TFSI$^-$-content IL electrolyte [56]. The imperfect compatibility of TFSI-based IL electrolytes with graphite anodes has been previously documented [57–59]. As shown in Table 1, the TFSI$^-$ molar ratio in the FT-13 IL electrolyte is as high as ~ 37%. We speculate that this contributed to the inadequate rate capability of both the LNMO and graphite electrodes. FSI$^-$ anions can generate a more protective and more conductive electrode/electrolyte interfacial film [33,34,60]; accordingly, a sufficient amount of FSI$^-$ in the IL electrolyte is crucial. The goal is to design an electrolyte composition that contains a high FSI$^-$/TFSI$^-$ ratio while limiting Al corrosion.

3.3. *Effects of Li$^+$/TFSI$^-$/FSI$^-$ molar ratio*

We increased the FSI$^-$/TFSI$^-$ ratio and modulated the Li$^+$ fraction in the electrolyte. To attain this design, LiTFSI at various concentrations was dissolved in the PMP − FSI IL. The obtained Li$^+$/TFSI$^-$/FSI$^-$ molar ratios are shown in Table 1. Given that the costs of LiTFSI and PMP–FSI IL are comparable, increasing the Li salt concentration does not really cause an economical concern. Fig. 6**(a)** shows the Raman spectra of the prepared IL electrolytes. At a low concentration of LiTFSI (i.e., 0.8 m), the FSI-related species are dominant and the free FSI$^-$ signal is noticeable. When the LiTFSI concentration is increased to 1.6 and 2.4 m, the Raman spectra shift toward a higher wavenumber. This can be attributed to the increased TFSI$^-$ content (TFSI$^-$ species are located at higher wavenumber positions compared to those of the corresponding FSI$^-$ species) and the promoted formation of CIP and AGG states of both FSI$^-$ and TFSI$^-$ due to the increased Li$^+$ fraction. **Fig. S4(a) and (b)** show the LSV and chronoamperometry data (at 5 V), respectively, of Al electrodes measured in various LiTFSI/PMP − FSI electrolytes. The oxidation current remarkably decreased with increasing LiTFSI concentration. The suppression of Al corrosion was confirmed by SEM inspection. As shown in **Fig. S5**, the integrity of the Al electrode remained high and no corrosion pits were found after the chronoamperometry measurement in the 2.4 m LiTFSI/PMP − FSI electrolyte. Fig. 6**(b)** compares the anodic

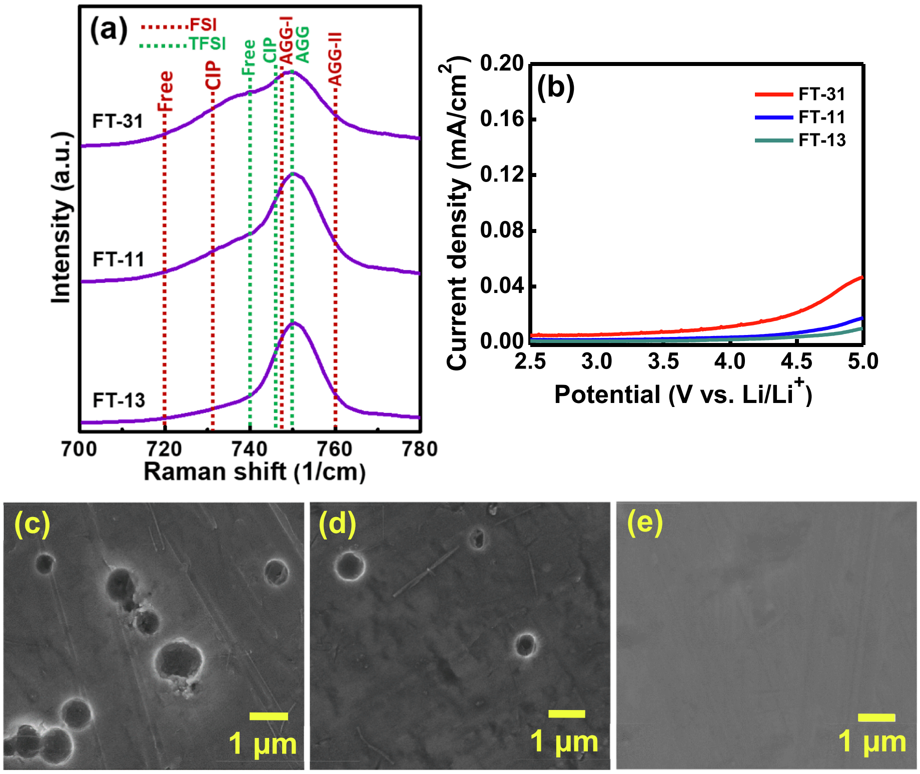

Fig. 4. (a) Raman spectra of electrolytes with various FSI$^-$/TFSI$^-$ molar ratio. (b) LSV curves of Al electrodes recorded in various electrolytes. SEM images of Al electrodes after chronoamperometry tests in (c) FT-31, (d) FT-11, and (e) FT-13 electrolytes.

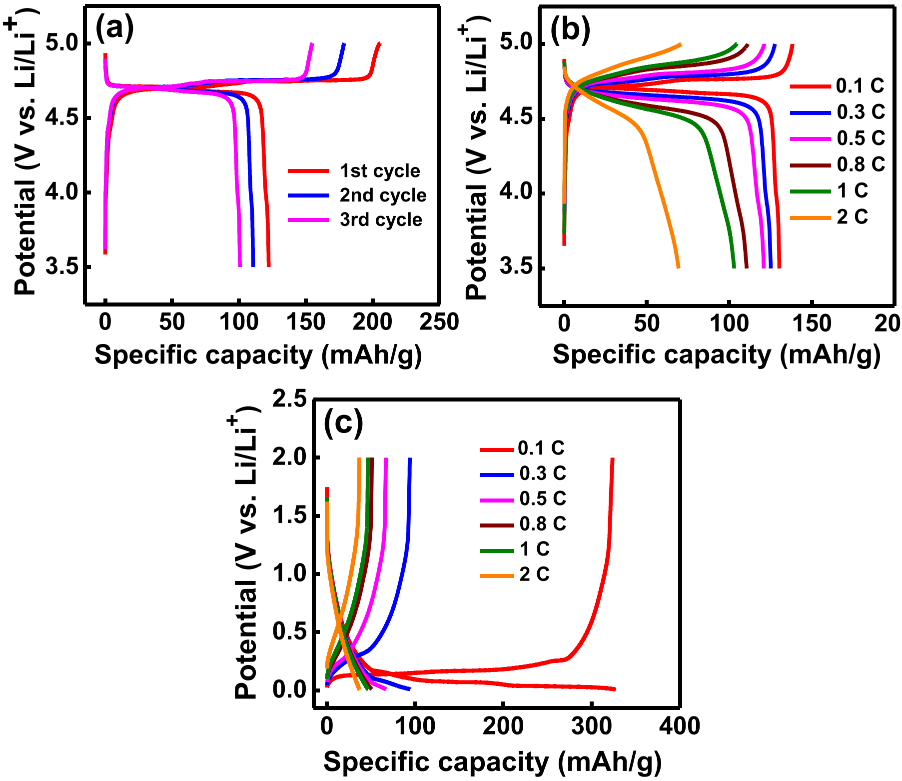

Fig. 5. Charge-discharge curves of LNMO half cells with (a) FT-11 and (b) FT-13 electrolytes. (c) Charge-discharge curves of graphite half cell with FT-13 electrolyte.

Table 1

Li^+, PMP^+, FSI^-, and $TFSI^-$ fractions for various IL electrolytes investigated in this study.

Electrolytes	Li^+	PMP^+	FSI^-	$TFSI^-$	Viscosity (cP)
0.8 m LiFSI/PMP–FSI	0.10	0.40	0.50	0	51
1.6 m LiFSI/PMP–FSI	0.17	0.33	0.50	0	79
2.4 m LiFSI/PMP–FSI	0.21	0.29	0.50	0	114
3.2 m LiFSI/PMP–FSI	0.25	0.25	0.50	0	176
FT-31	0.10	0.40	0.38	0.12	53
FT-11	0.11	0.39	0.25	0.25	80
FT-13	0.12	0.38	0.13	0.37	114
0.8 m LiTFSI/PMP–FSI	0.10	0.40	0.40	0.10	52
1.6 m LiTFSI/PMP–FSI	0.17	0.33	0.33	0.17	108
2.4 m LiTFSI/PMP–FSI	0.21	0.29	0.29	0.21	167

current densities of the Al electrodes measured at 5 V (vs. Li^+/Li) after 24 h in various IL electrolytes. Of note, the 2.4 m LiTFSI/PMP – FSI electrolyte most effectively minimizes Al dissolution while maintaining a sufficient $FSI^-/TFSI^-$ molar ratio (see Table 1). With an increased concentration of Li^+, the FSI^- anions are prone to be coordinated as the CIP and AGG states. As a consequence, it is not necessary to use a high fraction of $TFSI^-$ to mitigate electrolyte corrosivity. Fig. 6**(c)** shows the TGA data for the 2.4 m LiTFSI/PMP – FSI IL electrolyte. Two-step weight loss was observed, including decomposition of FSI-containing species at ~ 330 °C and decomposition of TFSI-containing species above 400 °C [53]. The FSI-related decomposition temperature is higher than that (~310 °C) found in Fig. 2**(b)**. This implies that different FSI^- coordination statuses could have different thermal stabilities, with the CIP and AGG states being more stable than free FSI^- anions. The inset in Fig. 6**(c)** confirms that the 2.4 m LiTFSI/PMP – FSI electrolyte is flame-retardant. The negligible volatility contributes to the high safety of this electrolyte for LIB applications.

Operation of the LNMO cell with the 0.8 m LiTFSI/PMP – FSI electrolyte failed, as shown in **Fig. S6(a)**. However, because Al dissolution decreased when the LiTFSI concentration was increased to 1.6 m, successful charge–discharge cycles of the LNMO cell were validated, as shown in **Fig. S6(b)**, although the CE was not high. Exceptional LNMO performance was obtained when the 2.4 m LiTFSI/PMP – FSI electrolyte was used. Fig. 7**(a)** shows that the reversible capacity of LNMO at 0.1C is 135 mAh g^{-1}, which is close to the theoretical capacity of 147 mAh g^{-1}. Even at 2C, a decent capacity of 100 mAh g^{-1} was attained at room temperature. The observed polarization of the charge and discharge curves is smaller than that found for the FT-13 cell. Fig. 7**(b)** compares the rate capability of the LNMO cells with the FT-13 and 2.4 m LiTFSI/PMP – FSI electrolytes, for which 54% and 74% of the capacities measured at 0.1C were retained at 2C, respectively. The much improved high-rate performance of the latter cell can be ascribed to the higher Li^+ fraction and higher $FSI^-/TFSI^-$ molar ratio of the IL electrolyte. The poor rate capability of the 1 M LiTFSI/PMP – TFSI cell shown in **Fig. S7** supports this argument. **Fig. S8** shows the electrochemical impedance spectroscopy data of the FT-13 and 2.4 m LiTFSI/PMP – FSI cells. The Nyquist plots consist of a semicircle at high frequency and a sloping line at low frequency, which can be characterized by the equivalent circuit shown in the figure inset, where R_e, R_{ct}, C_{int}, and Z_W are the electrolyte resistance, interfacial charge transfer resistance, interfacial capacitance, and Warburg impedance associated with Li^+ diffusion within the electrode, respectively. The calculated electrolyte conductivity values are 1.4 (for FT-13) and 1.2 mS cm^{-1} (for 2.4 m LiTFSI/PMP – FSI), respectively. However, the R_{ct} values, the dominant impedance of the cells, are 130 and 62 Ω, respectively, explaining the superior rate capability of the latter cells. Fig. 7**(c)** shows the cell cycling stability data for the FT-13 and 2.4 m LiTFSI/PMP – FSI cells recorded at 1C. After 200 charge–discharge cycles, the capacity retention ratios were 72% and 88%, respectively. The superior cyclability of the latter cell is related to less Al current collector corrosion, as illustrated in Fig. 6**(b)**.

Fig. 7**(d)** shows the charge–discharge curves of the graphite half cell with 2.4 m LiTFSI/PMP – FSI electrolytes measured at various C rates. The reversible capacity at 0.1C was ~ 340 mAh g^{-1}, decreasing to ~ 100

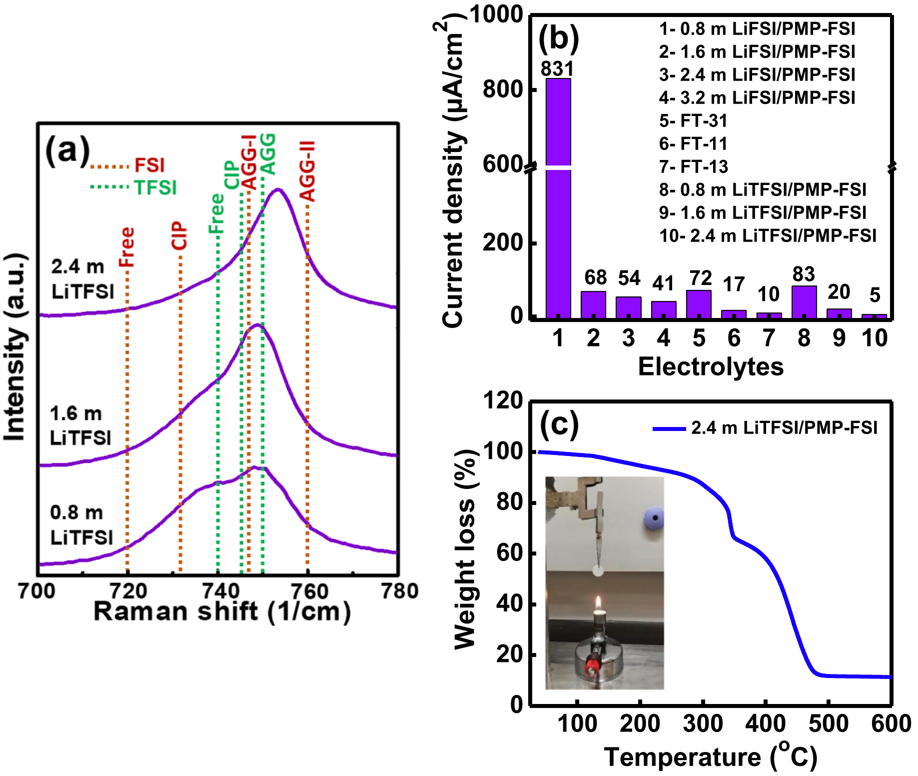

Fig. 6. (a) Raman spectra of LiTFSI/PMP–FSI electrolytes with various concentrations of LiTFSI. (b) Side reaction current densities of Al electrodes after being held at 5 V for 24 h in various electrolytes. (c) TGA data and flammability of 2.4 m LiTFSI/PMP–FSI electrolyte.

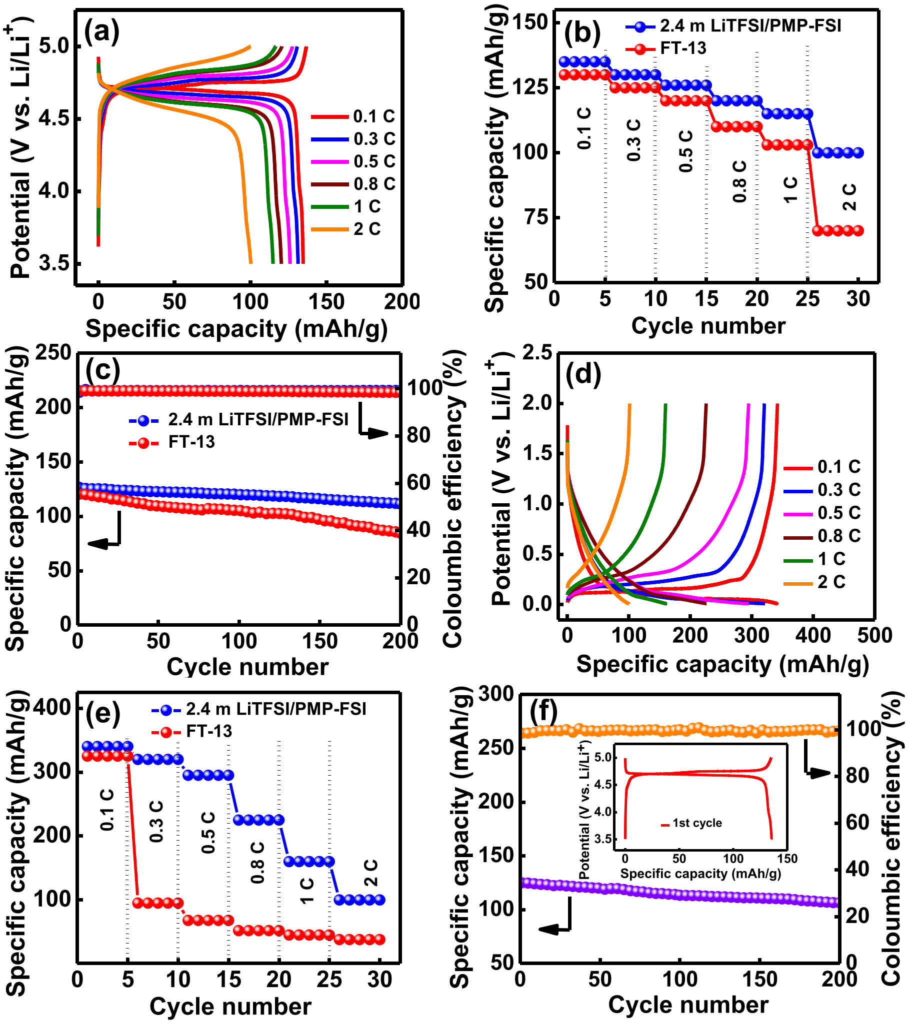

Fig. 7. (a) Charge–discharge curves of LNMO half cell with 2.4 m LiTFSI/PMP − FSI electrolyte. Comparative (b) rate capability and (c) cycling stability (at 1C) of LNMO cells with two electrolytes. (d) Charge–discharge curves of graphite half cell with 2.4 m LiTFSI/PMP − FSI electrolyte. (e) Comparative rate capability of graphite cells with two electrolytes. (f) Charge–discharge curves and cyclic stability data of graphite//LNMO full cell with 2.4 m LiTFSI/PMP − FSI electrolyte.

mAh g^{-1} at 2C. As shown in Fig. 7**(e)**, the rate capability of this graphite cell is considerably higher than that with the FT-13 electrolyte. At 2C, 11% and 29% of the capacities measured at 0.1C were retained, respectively, with the FT-13 and 2.4 m LiTFSI/PMP − FSI electrolytes. A previous study reported that TFSI$^-$ anions are unable to form a robust and conductive SEI layer, leading to unsatisfactory anode performance [61]. Our data in **Fig. S9** also indicate that a graphite electrode shows unstable lithiation/delithiation behavior with a low capacity in the 1 M LiTFSI/PMP − TFSI electrolyte. The relatively high FSI$^-$/TFSI$^-$ ratio (29 mol% vs. 21 mol%; see Table 1) of the 2.4 m LiTFSI/PMP − FSI IL electrolyte is responsible for the upgraded SEI and thus the superior charge–discharge performance of the graphite electrode. **Fig. S10** shows the contact angles between the 2.4 m LiTFSI/PMP − FSI IL and the LNMO and graphite electrodes. The high wettability was confirmed. We expect that this electrolyte is suitable for high-voltage LIBs, although the charge–discharge properties of specific cathodes and anodes may need further investigations.

The solubility of LiTFSI in PMP − FSI IL is approximately 2.8 m. However, we found that both the LNMO and graphite electrodes showed inferior rate capability with this LiTFSI-saturated electrolyte, presumably due to its high viscosity and excessive TFSI$^-$ content. In addition, lithium bis(oxalato)borate and lithium difluoro(oxalato)borate salts were also attempted. Unfortunately, their solubility in PMP–FSI IL is limited (i.e. ~ 1 M) and the electrolyte viscosity is too high to ensure good charge–discharge performance. The feasibility of the 2.4 m LiTFSI/PMP − FSI IL electrolyte was further validated in a graphite//LNMO full cell; the data obtained are shown in Fig. 7**(f)**. The figure inset shows that the charge–discharge capacity at 0.1C is approximately 135 mAh g^{-1} (based on LNMO; or ~ 93 mAh g^{-1} based on both LNMO and graphite). This graphite//2.4 m LiTFSI/PMP − FSI IL//LNMO cell exhibits high reversibility and retains up to ~ 85% of its initial capacity after 200 cycles at 0.5C. **Fig. S11(a) and (b)** show the charge–discharge performance of this full cell measured at various rates. As shown, 0.5C charging is feasible. A higher charging rate can cause noticeable discharge capacity decrease, as compared in **Table S1**. **Fig. S12** shows the post-morterm SEM image of the cycled LNMO electrode. Although a thin covering layer on the electrode was observed (which is supposed to be a reason for the capacity decay), the LNMO microstructure can be preserved. The high cycling stability can be attributed to the good compatibility of the proposed electrolyte toward both the graphite anode and the high-voltage LNMO cathode. We believe that the proposed electrolyte composition and its design concept have great potential to be used for high-energy–density and high-safety LIBs.

4. Conclusions

An organic-solvent-free FSI$^-$-based IL electrolyte with high thermal stability and non-flammability was for the first time successfully used for a high-voltage LNMO cell. We found that simply increasing the LiFSI concentration (even to 3.2 m) in the PMP − FSI IL electrolyte cannot effectively inhibit Al corrosion, leading to a low charge–discharge CE of the LNMO electrode. When $TFSI^-$ anions were incorporated in the electrolyte, Al dissolution was suppressed. However, the high $TFSI^-/FSI^-$ molar ratio led to a limited rate capability of the LNMO cathode and unsatisfactory compatibility with the graphite anode. We thus proposed a $Li^+/TFSI^-/FSI^-$ modulation concept to optimize the IL electrolyte. An increase in the Li^+ fraction reduced the amount of free FSI^- anions, which are prone to attack Al. Therefore, a high $TFSI^-$ ratio is not required. The optimal 2.4 m LiTFSI/PMP − FSI IL electrolyte minimizes the side reaction current of the Al electrode at 5 V. Moreover, the relatively high Li^+ and FSI^- ratios ensure superior charge–discharge properties of both the LNMO and graphite electrodes. A high reversible capacity of approximately 135 mAh g^{-1} at 0.1C based on LNMO was verified for a graphite//LNMO full cell. This cell was able to retain ∼ 85% of its initial capacity after 200 cycles. These results can guide the development of FSI^--based IL electrolytes for high-reliability battery applications.

Declaration of Competing Interest

The authors declare that they have no known competing financial interests or personal relationships that could have appeared to influence the work reported in this paper.

Acknowledgments

The financial support provided for this work by the Ministry of Science and Technology (MOST) of Taiwan is gratefully appreciated.

Appendix A. Supplementary data

Supplementary data to this article can be found online at https://doi.org/10.1016/j.cej.2021.128904.

References

[1] C. Liu, F. Li, L.P. Ma, H.M. Cheng, Advanced material for energy storage, Adv. Mater. 22 (2010) E28–62.

[2] H.D. Yoo, E. Markevich, G. Salitra, D. Sharon, D. Aurbach, On the challenge of developing advanced technologies for electrochemical energy storage and conversion, Mater. Today 17 (2014) 110–121.

[3] T.M. Gür, Review of electrical energy storage technologies, materials and systems: Challenges and prospects for large-scale grid storage, Energy Environ. Sci. 11 (2018) 2696–2767.

[4] F. Wu, J. Maier, Y. Yu, Guidelines and trends for next-generation rechargeable lithium and lithium-ion batteries, Chem. Soc. Rev. 49 (2020) 1569–1614.

[5] C. Liu, Z.G. Neale, G. Cao, Understanding electrochemical potentials of cathode materials in rechargeable batteries, Mater. Today 19 (2016) 109–123.

[6] A. Manthiram, J.C. Knight, S.T. Myung, S.M. Oh, Y.K. Sun, Nickel-rich and lithium-rich layered oxide cathodes: Progress and perspectives, Adv. Energy Mater. 6 (2016), 151010.

[7] M. Hu, X. Pang, Z. Zhou, Recent progress in high-voltage lithium ion batteries, J. Power Sources 237 (2013) 229–242.

[8] Y. Huang, Y. Dong, S. Li, J. Lee, C. Wang, Z. Zhu, W. Xue, Y. Li, J. Li, Lithium manganese spinel cathodes for lithium-ion batteries, Adv. Energy Mater. 11 (2021) 2000997.

[9] K. Xu, Electrolytes and interphases in Li-ion batteries and beyond, Chem. Rev. 114 (2014) 11503–11618.

[10] Z. Zou, H. Xu, H. Zhang, Y. Tang, G. Cui, Electrolyte therapy for improving the performance of $LiMn_{1.5}Ni_{0.5}O_4$ cathodes assembled lithium-ion batteries, ACS Appl. Mater. Interfaces 12 (2020) 21368–21385.

[11] Y. Yu, P. Karayaylali, Y. Katayama, L. Giordano, M. Gauthier, F. Maglia, R. Jung, I. Lund, Y.S. Horn, Coupled $LiPF_6$ decomposition and carbonate dehydrogenation enhanced by highly covalent metal oxides in high-energy Li-ion batteries, J. Phys. Chem. C 122 (2018) 27368–27382.

[12] T. Kawamura, S. Okada, J.I. Yamaki, Decomposition reaction of $LiPF_6$-based electrolytes for lithium ion cells, J. Power Sources 156 (2006) 547–554.

[13] J.B. Goodenough, Y. Kim, Challenges for rechargeable Li batteries, Chem. Mater. 22 (2010) 587–603.

[14] H. Yang, G.V. Zhuang, P.N. Ross, Thermal stability of $LiPF_6$ salt and Li-ion battery electrolytes containing $LiPF_6$, J. Power Sources 161 (2006) 573–579.

[15] S. Solchenbach, M. Metzger, M. Egawa, H. Beyer, H.A. Gasteiger, Quantification of PF_5 and POF_3 from side reactions of $LiPF_6$ in Li-ion batteries, J. Electrochem. Soc. 165 (2018) A3022–A3028.

[16] M. Watanabe, M.L. Thomas, S. Zhang, K. Ueno, T. Yasuda, K. Dokko, Application of ionic liquids to energy storage and conversion materials and devices, Chem. Rev. 117 (2017) 7190–7239.

[17] M. Armand, F. Endres, D.R. MacFarlane, H. Ohno, B. Scrosati, Ionic-liquid materials for the electrochemical challenges of the future, Nat. Mater. 8 (2009) 621–629.

[18] D.R. MacFarlane, N. Tachikawa, M. Forsyth, J.M. Pringle, P.C. Howlett, G. D. Elliott, J.H. Davis, M. Watanabe, P. Simon, C.A. Angell, Energy applications of ionic liquids, Energy Environ. Sci. 7 (2014) 232–250.

[19] M. Shi, P. Xiao, J. Lang, C. Yan, X. Yan, Porous g-C_3N_4 and MXene dual-confined FeOOH quantum dots for superior energy storage in an ionic liquid, Adv. Sci. 7 (2020) 1901975.

[20] Y. Liu, M. Narayanasamy, C. Yang, M. Shi, W. Xie, H. Wu, C. Yan, H. Hou, Z. Guo, High-performance coaxial wire-shaped supercapacitors using ionogel electrolyte toward sustainable energy system, J. Mater. Res. 34 (2019) 3030–3039.

[21] Q. Yang, Z. Zhang, X.G. Sun, Y.S. Hu, H. Xing, S. Dai, Ionic liquids and derived materials for lithium and sodium batteries, Chem. Soc. Rev. 47 (2018) 2020–2064.

[22] E. Bordes, L. Douce, E.L. Quitevis, A.A.H. Padua, M.C. Gomes, Ionic liquids at the surface of graphite: Wettability and structure, J. Chem. Phys. 148 (2018), 193840.

[23] J. Patra, P.P. Dahiya, C.J. Tseng, J. Fang, Y.W. Lin, S. Basu, S.B. Majumder, J. K. Chang, Electrochemical performance of 0.5 Li_2MnO_3–0.5 Li $(Mn_{0.375}Ni_{0.375}Co_{0.25})O_2$ composite cathode in pyrrolidinium-based ionic liquid electrolytes, J. Power Sources 294 (2015) 22–30.

[24] P.C. Rath, C.J. Wu, J. Patra, J. Li, T.C. Lee, T.J. Yeh, J.K. Chang, Hybrid electrolyte enables safe and practical 5 V $LiNi_{0.5}Mn_{1.5}O_4$ batteries, J. Mater. Chem. A. 7 (2019) 16516–16525.

[25] C.J. Wu, P.C. Rath, J. Patra, D. Bresser, S. Passerini, B. Umesh, Q.F. Dong, T.C. Lee, J.K. Chang, Composition modulation of ionic liquid hybrid electrolyte for 5 V lithium-ion batteries, ACS Appl. Mater. Interfaces 11 (2019) 42049–42056.

[26] C. Arbizzani, G. Gabrielli, M. Mastragostino, Thermal stability and flammability of electrolytes for lithium-ion batteries, J. Power Sources 196 (2011) 4801–4805.

[27] I. Quinzeni, S. Ferrari, E. Quartarone, C. Tomasi, M. Fagnoni, P. Mustarelli, Li-doped mixtures of alkoxy-N-methylpyrrolidinium bis(trifluoromethanesulfonyl)-imide and organic carbonates as safe liquid electrolytes for lithium batteries, J. Power Sources 237 (2013) 204–209.

[28] X. Cao, X. He, J. Wang, H. Liu, S. Roser, B.R. Rad, M. Evertz, B. Streipert, J. Li, R. Wagner, M. Winter, I.C. Laskovic, High voltage $LiNi_{0.5}Mn_{1.5}O_4$ /$Li_4Ti_5O_{12}$ lithium-ion cells at elevated temperatures: Carbonate-versus ionic liquid-based electrolytes, ACS Appl. Mater. Interfaces 8 (2016) 25971–25978.

[29] N. Wongittharom, T.C. Lee, I.M. Hung, S.W. Lee, Y.C. Wang, J.K. Chang, Ionic liquid electrolytes for high-voltage rechargeable Li/ $LiNi_{0.5}Mn_{1.5}O_4$ cells, J. Mater. Chem. A 2 (2014) 3613–3620.

[30] Q. Liu, W. Jiang, M.J.P. Munoz, Y. Liu, Z. Yang, I. Bloom, T.L. Dzwiniel, Y. Li, K. Z. Pupek, Z. Zhang, Stabilized electrode/electrolyte interphase by a saturated ionic liquid electrolyte for high-voltage NMC 532/Si-graphite cells, ACS Appl. Mater. Interfaces 12 (2020) 23035–23045.

[31] N. Wongittharom, T.C. Lee, C.H. Hsu, G.T.K. Fey, K.P. Huang, J.K. Chang, Electrochemical performance of rechargeable Li/$LiFePO_4$ cells with ionic liquid electrolyte: Effects of Li salt at 25 °C and 50 °C, J. Power Sources 240 (2013) 676–682.

[32] H.F. Xiang, B. Yin, H. Wang, H.W. Lin, X.W. Ge, S. Xie, C.H. Chen, Improving electrochemical properties of room temperature ionic liquid (RTIL) based electrolyte for Li-ion batteries, Electrochim. Acta 55 (2010) 5204–5209.

[33] M. Yamagata, Y. Matsui, T. Sugimoto, M. Kikuta, T. Higashizaki, M. Kono, M. Ishikawa, High-performance graphite negative electrode in a bis(fluorosulfonyl) imide-based ionic liquid, J. Power Sources 227 (2013) 60–64.

[34] K. Beltrop, X. Qi, T. Hering, S. Röser, M. Winter, T. Placke, Enabling bis (fluorosulfonyl)imide-based ionic liquid electrolytes for application in dual-ion batteries, J. Power Sources 373 (2018) 193–202.

[35] N. Salem, S. Zavorine, D. Nucciarone, K. Whitbread, M. Moser, Y.A. Lebdeh, Physical and electrochemical properties of some phosphonium-based ionic liquids and the performance of their electrolytes in lithium-ion batteries, J. Electrochem. Soc. 164 (2017) H5202–H5209.

[36] H. Zhang, W. Qu, N. Chen, Y. Huang, L. Li, F. Wu, R. Chen, Ionic liquid electrolyte with highly concentrated LiTFSI for lithium metal batteries, Electrochim. Acta 285 (2018) 78–85.

[37] S. Yamaguchi, M.Y. Fujita, Y. Takeoka, M. Rikukawa, Effect of a pyrrolidinium zwitterion on charge/discharge cycle properties of Li/$LiCoO_2$ and graphite/Li cells containing an ionic liquid electrolyte, J. Power Sources 331 (2016) 308–314.

[38] A. Heist, S.H. Lee, Improved stability and rate capability of ionic liquid electrolyte with high concentration of LiFSI, J. Electrochem. Soc. 166 (2019) A1860–A1866.

[39] Q. Liu, T.L. Dzwiniel, K.Z. Pupek, Z. Zhang, Corrosion/passivation behavior of concentrated ionic liquid electrolytes and its impact on the Li-ion battery performance, J. Electrochem. Soc. 166 (2019) A3959–A3964.

[40] E. Cho, J. Mun, O.B. Chae, O.M. Kwon, H.T. Kim, J.H. Ryu, Y.G. Kim, S.M. Oh, Corrosion/passivation of aluminum current collector in bis(fluorosulfonyl)imide-based ionic liquid for lithium-ion batteries, Electrochem. Commun. 22 (2012) 1–3.

[41] R.S. Kühnel, A. Balducci, Comparison of the anodic behavior of aluminum current collectors in imide-based ionic liquids and consequences on the stability of high voltage supercapacitors, J. Power Sources 249 (2014) 163–171.

[42] W.K. Pang, H.F. Lin, V.K. Peterson, C.Z. Lu, C.E. Liu, S.C. Liao, J.M. Chen, Enhanced rate-capability and cycling-stability of 5 V SiO_2-and polyimide-coated

cation ordered $LiNi_{0.5}Mn_{1.5}O_4$ lithium-ion battery positive electrodes, J. Phys. Chem. C 121 (2017) 3680–3689.

[43] J.H. Kim, A. Huq, M. Chi, N.P.W. Pieczonka, E. Lee, C.A. Bridges, M.M. Tessema, A. Manthiram, K.A. Persson, B.R. Powell, Integrated nano-domains of disordered and ordered spinel phases in $LiNi_{0.5}Mn_{1.5}O_4$ for Li-ion batteries, Chem. Mater. 26 (2014) 4377–4386.

[44] J.H. Kim, S.T. Myung, C.S. Yoon, S.G. Kang, Y.K. Sun, Comparative study of $LiNi_{0.5}Mn_{1.5}O_4$-δ and $LiNi_{0.5}Mn_{1.5}O_4$ cathodes having two crystallographic structures: Fd3m and $P4_332$, Chem. Mater. 16 (2004) 906–914.

[45] A.K. Haridas, C.S. Sharma, T.N. Rao, Caterpillar-like sub-micron $LiNi_{0.5}Mn_{1.5}O_4$ structures with site disorder and excess Mn^{3+} as high performance cathode material for lithium ion batteries, Electrochim. Acta 212 (2016) 500–509.

[46] N.P.W. Pieczonka, Z. Liu, P. Lu, K.L. Olson, J. Moote, B.R. Powell, J.H. Kim, Understanding transition-metal dissolution behavior in $LiNi_{0.5}Mn_{1.5}O_4$ high-voltage spinel for lithium ion batteries, J. Phys. Chem. C 117 (2013) 15947–15957.

[47] I.A. Shkrob, T.W. Marin, Y. Zhu, D.P. Abraham, Why bis(fluorosulfonyl)imide is a “magic anion” for electrochemistry, J. Phys. Chem. C 118 (2014) 19661–19671.

[48] K. Kimura, J. Motomatsu, Y. Tominaga, Correlation between solvation structure and ion-conductive behavior of concentrated poly(ethylene carbonate)-based electrolytes, J. Phys. Chem. C 120 (2016) 12385–12391.

[49] Z.H. Chang, J.T. Wang, Z.H. Wu, M. Gao, S.J. Wu, S.G. Lu, The electrochemical performance of silicon nanoparticles in concentrated electrolyte, ChemSusChem 11 (2018) 1787–1796.

[50] S.D. Han, O. Borodin, D.M. Seo, Z.B. Zhou, W.A. Henderson, Electrolyte solvation and ionic association V. Acetonitrile-lithium bis(fluorosulfonyl)imide (LiFSI) mixtures, J. Electrochem. Soc. 161 (2014) A2042–A2053.

[51] A.K. Chan, R. Tatara, S. Feng, P. Karayaylali, J. Lopez, I.E.L. Stephens, Y.S. Horn, Concentrated electrolytes for enhanced stability of Al-Alloy negative electrodes in Li-ion batteries, J. Electrochem. Soc. 166 (2019) A1867–A1874.

[52] Y. Yamada, K. Furukawa, K. Sodeyama, K. Kikuchi, M. Yaegashi, Y. Tateyama, A. Yamada, Unusual stability of acetonitrile-based superconcentrated electrolytes for fast-charging lithium-ion batteries, J. Am. Chem. Soc. 136 (2014) 5039–5046.

[53] M. Kerner, N. Plylahan, J. Scheers, P. Johansson, Ionic liquid based lithium battery electrolytes: Fundamental benefits of utilizing both TFSI and FSI anions? Phys Chem Chem Phys 17 (2015) 19569–19581.

[54] C. Peng, L. Yang, Z. Zhang, K. Tachibana, Y. Yang, S. Zhao, Investigation of the anodic behavior of Al current collector in room temperature ionic liquid electrolytes, Electrochim. Acta 53 (2008) 4764–4772.

[55] R.S. Kühnel, M. Lübke, M. Winter, S. Passerini, A. Balducci, Suppression of aluminum current collector corrosion in ionic liquid containing electrolytes, J. Power Sources 214 (2012) 178–184.

[56] H. Zheng, K. Jiang, T. Abe, Z. Ogumi, Electrochemical intercalation of lithium into a natural graphite anode in quaternary ammonium-based ionic liquid electrolytes, Carbon 44 (2006) 203–210.

[57] M. Holzapfel, C. Jost, P. Novak, Stable cycling of graphite in an ionic liquid based electrolyte, ChemComm (2004) 2098–2099.

[58] S. Seki, Y. Kobayashi, H. Miyashiro, Y. Ohno, Y. Mita, N. Terada, Compatibility of N-Methyl-N-propylpyrrolidinium cation room-temperature ionic liquid electrolytes and graphite electrodes, J. Phys. Chem. C 112 (2008) 16708–16713.

[59] S. Rothermel, P. Meister, O. Fromm, J. Huesker, H.W. Meyer, M. Winter, T. Placke, Study of the electrochemical behavior of dual-graphite cells using ionic liquid-based electrolytes, ECS Trans. 58 (2014) 15–25.

[60] A. Guerfi, S. Duchesne, Y. Kobayashi, A. Vijh, K. Zaghib, $LiFePO_4$ and graphite electrodes with ionic liquids based on bis(fluorosulfonyl)imide $(FSI)^-$ for Li-ion batteries, J. Power Sources 175 (2008) 866–873.

[61] N. Nakatani, K. Kishida, K. Nakagawa, Effect of SEI component on graphite electrode performance for Li-ion battery using ionic liquid electrolyte, J. Electrochem. Soc. 165 (2018) A1621–A1625.